Bulletin of the Seismological Society of America, Vol. 97, No. 1A, pp. S86–S102, January 2007, doi: 10.1785/0120050609

Ⓔ

Coseismic Slip Distributions of the 26 December 2004 Sumatra–Andaman and 28 March 2005 Nias Earthquakes from GPS Static Offsets

by Paramesh Banerjee, Fred Pollitz, B. Nagarajan, and Roland Bürgmann

Abstract Static offsets produced by the 26 December 2004 M ~9 Sumatra–Andaman earthquake as measured by Global Positioning System (GPS) reveal a large amount of slip along the entire ≳1300 km-long rupture. Most seismic slip inversions place little slip on the Andaman segment, whereas both near-field and far-field GPS offsets demand large slip on the Andaman segment. We compile available datasets of the static offset to render a more detailed picture of the static-slip distribution. We construct geodetic offsets such that postearthquake positions of continuous GPS sites are reckoned to a time 1 day after the earthquake and campaign GPS sites are similarly corrected for postseismic motions. The newly revised slip distribution (M_w 9.22) reveals substantial segmentation of slip along the Andaman Islands, with the southern quarter slipping ~15 m in unison with the adjacent Nicobar and northern Sumatran segments of length ~700 km. We infer a small excess of geodetic moment relative to the seismic moment. A similar compilation of GPS offsets from the 28 March 2005 Nias earthquake is well explained with dip slip averaging several meters ($M_w = 8.66$) distributed primarily at depths greater than 20 km.

Online material: Offset estimation procedure, comparison of results to other studies and simpler solutions, and tables of coseismic offsets.

Introduction

The 26 December 2004 M ~9 Sumatra–Andaman earthquake and 28 March 2005 M 8.7 Nias earthquake ruptured portions of the Sumatra and Sunda subduction zones over lengths of ~1500 km and ~400 km, respectively (Fig. 1). The slip distribution of the Sumatra–Andaman earthquake has been estimated from seismic waves (Ammon *et al.*, 2005; Lay *et al.*, 2005), static offsets (Banerjee *et al.*, 2005; Vigny *et al.*, 2005; Subarya *et al.*, 2006), and joint seismic-geodetic data (Chlieh *et al.*, 2007). The overall size of the earthquake has been further constrained by Earth's free oscillations (Park *et al.*, 2005; Stein and Okal, 2005). Each study makes use of a different frequency band, and as first noted by Stein and Okal (2005) and subsequent investigators, the apparent earthquake size increases with period. Banerjee *et al.* (2005) found that the effectively zero-frequency static offsets, based on a combination of preseismic and 0- to 5-day postseismic Global Positioning System (GPS) measurements, apparently required an earthquake size of an order 30% larger than that detected by long-period free oscillations, independent of the strong correlation of the estimated moment and dip in both seismic and geodetic estimates of magnitude. However, the size of the source required to explain free oscillation measurements increases when a finite source time function, rather than an impulsive source, is used because of phase cancellation (Park *et al.*, 2005). The free oscillation measurements are well explained with a source of ~600-sec duration over a broad range of frequencies (Park *et al.*, 2005), with a seismic moment of 6.5×10^{22} N m, the same as that inferred by Banerjee *et al.* (2005). The excellent fit of a distributed slip model to joint seismic and geodetic datasets (Chlieh *et al.*, 2007) shows directly that the two types of data are essentially compatible and yield the same earthquake size.

The seismic investigations have used large seismic datasets, resulting in detailed slip models of the earthquake at seismic periods up to 1 hr. Investigations based on the static offsets cannot resolve the temporal evolution of slip, but allow a better picture of the net coseismic slip distribution. They are also ideally suited to detect slip at a timescale much greater than the seismically detected rupture duration. However, previous investigations of the static offset are based on measurements that typically include several days of postseismic motions. The very rapid motions obtained by continuous GPS measurements in the days following the earthquake (e.g., Vigny *et al.*, 2005), when integrated over several days, are generally a substantial fraction of the actual coseismic offset. The purpose of this article is to expand and revise the 26 December 2004 static-offset dataset of Baner-

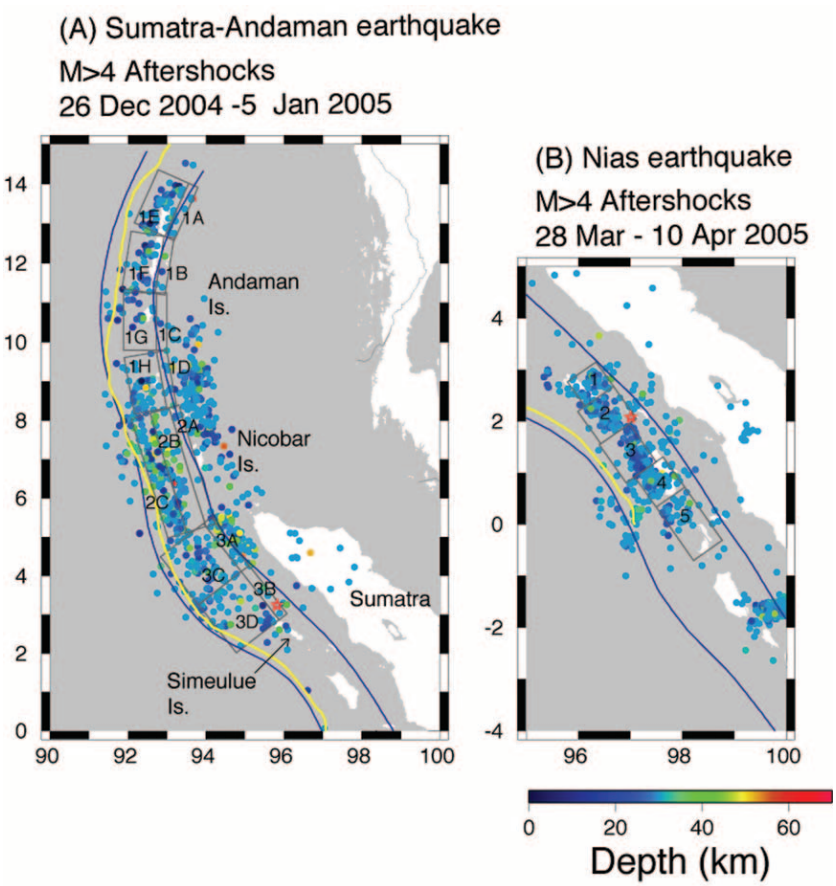

Figure 1. Aftershock activity following the (a) 2004 Sumatra–Andaman and (b) 2005 Nias earthquakes, from the National Earthquake Information Center (NEIC) catalog. Superimposed are the fault planes used in dislocation modeling of the two earthquakes, from Tables S1 and S4, identified by the numerals. Fault labels 1, 2, and 3 identify subsegments that are loosely referred to as Andaman, Nicobar, and Sumatran segments, respectively. Dark blue curves are the 0 and 50 km slab depth contours of Gudmundsson and Sambridge (1998). Yellow curve is the trench axis determined by Curray (2005).

jee *et al.* (2005) to afford a more detailed picture of the net coseismic slip distribution. Where possible we apply corrections for postseismic offsets to render a clearer picture of the coseismic offset. We conduct a similar analysis of static offsets from the 28 March 2005 Nias earthquake to derive a simple slip distribution consistent with applicable geodetic data as well as seismotectonic constraints.

26 December 2004 Data Set

The GPS datasets of Banerjee *et al.* (2005) (their table S1) and Vigny *et al.* (2005) (their table 1) consist of horizontal velocity vectors estimated at 41 and 86 continuously operating sites (CGPS), respectively. We have expanded the dataset analyzed by Banerjee *et al.* (2005) to include 11 more sites belonging to various regional CGPS networks and 11 sites surveyed in campaign-mode (SGPS) before and after the event by the Survey of India (SOI) (Gahalaut *et al.*, 2006). GPS data from the CGPS sites were processed with the GAMIT/GLOBK software package (Herring, 2005; King and Bock, 2005) to produce time series of station coordinates in the ITRF-2000 reference frame. We used 18 global IGS GPS stations to implement the ITRF-2000 reference frame in the GPS analysis. Stations used to define the reference frame are >4500 km from the earthquake rupture. Time series at continuous GPS site PHKT is shown in Figure 2; time series at several other sites are shown in Ⓔ Figure S1 in the electronic edition of BSSA. Coseismic offsets of the CGPS sites are estimated by, first, determining the best-fitting straight lines to 18-day preseismic and 9-day postseismic portions of the time series; second, choosing a time t_0 on the preseismic line segment just prior to the earthquake and a time t_1 on the postseismic line segment just after the earthquake. Red and green line segments in Figure 2 illustrate line-segment fits obtained with the first step in the preseismic and postseismic intervals, respectively. When fewer than 18 days or 9 days of observations are available during the preseismic or postseismic epochs, respectively, then as many days as possible are used.

Ideally the separation between t_0 and t_1 should be only a few minutes, the duration of the seismically detected part of the earthquake (e.g., Ammon *et al.*, 2005). However, suggestions of slow slip lasting on the order of one hour (Bilham *et al.*, 2005; Stein and Okal, 2005) or longer (Banerjee *et al.*, 2005) suggest that t_1 be chosen such that the earthquake "duration" $t_1 - t_0$ be somewhat greater than one hour. We find that offsets estimated in this fashion are very similar for durations of $t_1 - t_0 = 1$ day and 2.5 days. The maximum slope of the first 9-days postseismic time series is -1.36 mm/day for the east component of PHKT, corresponding to 2 mm westward movement between postseismic days 1 and 2.5 after the earthquake, and slopes at all other

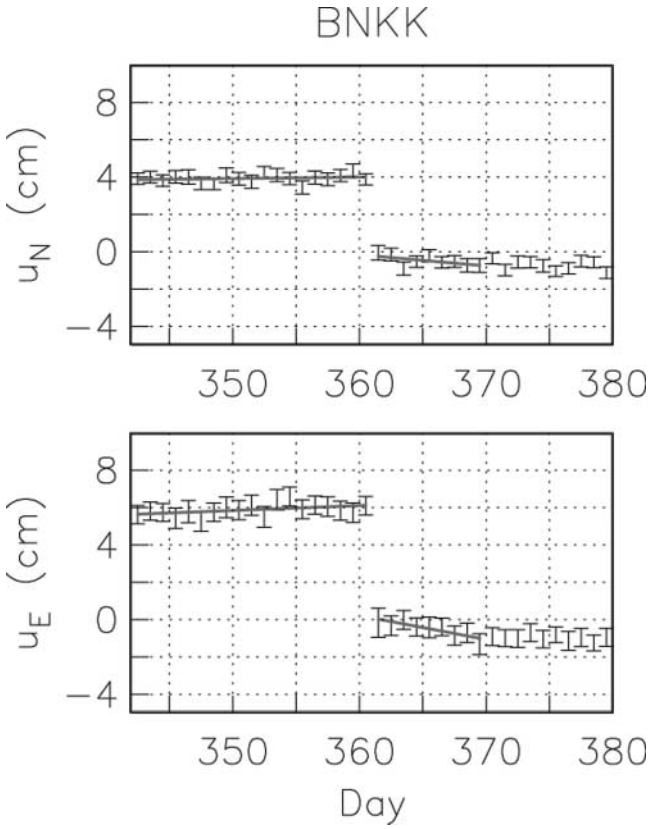

Figure 2. Observed GPS time series following the 26 December 2004 earthquake with $1-\sigma$ errors at continuous GPS site PHKT (site location in Fig. 3). u_E and u_N refer to east- and northward displacement, respectively. Day numbers refer to the year 2004. Superimposed in thick gray are the straight-line fits to 18-day portions of the preseismic and 9-day portions of the postseismic time series.

sites are much smaller (Ⓔ Figure S1 in the electronic edition). Thus we consider a duration of $t_1 - t_0 = 1$ day as a satisfactory choice for capturing essentially all of the coseismic signal without introducing much postseismic signal, which could arise from afterslip, viscoelastic relaxation, etc. The complete set of 53 coseismic horizontal displacement vectors derived in this study from our analysis of CGPS measurements is given in Ⓔ Table S1 in the electronic edition and plotted in Figure 3. We append an additional 55 displacement vectors from Vigny *et al.* (2005), corrected for postseismic displacements as explained Ⓔ in the supplement in the electronic edition. These are presented in Ⓔ Table S2 in the electronic edition and are shown by the blue vectors in Figure 3. Together with our newly determined offsets, this comprises a total of 108 far-field GPS static offsets.

The SOI carried out GPS campaign measurements of 13 survey points on the Andaman and Nicobar Islands in March 2004, 12 of which were resurveyed after the 26 December 2004 event (Gahalaut *et al.*, 2006). We have processed these data using the approach described previously and estimated their horizontal and vertical offsets (Ⓔ see Table S3 in the electronic edition). (The tabulated offsets include a small correction for postseismic motions as explained subsequently and listed in Ⓔ Table S3 in the electronic edition.) We appended an additional three-dimensional offset at Car Nicobar supplied by table 1 of Jade *et al.* (2005). These offsets are plotted in Figures 4 and 5. The campaign measurements were collected during the period 10 to 28 days following the earthquake and include 264 to 300 days of interseismic deformation prior to the event. They therefore include the effects of an unknown amount of afterslip and a small amount of pre-earthquake deformation. Subarya *et al.* (2006) present campaign measurements from northern Sumatra that also span the earthquake and about 1.5 months of postseismic deformation (their supplemental tables S1 and S2), which we also include in our analysis.

The question arises as to how much postseismic motion is present in the SGPS measurements from the Andaman Islands and northern Sumatra. Guidance is provided by CGPS measurements. Figure 6 shows estimated postseismic motions from 1 to 50 days after the earthquake at several CGPS sites. This includes postseismic time series at a new CGPS site CAR2 spanning the time period from 25 to 55 days after the earthquake, which constrains the postseismic motions in its locality near Port Blair (Paul *et al.*, 2005). The extrapolation of this motion to the period 1 to 50 days after the earthquake, using a $\log(t)$ dependence, is about 33 cm toward the west-southwest (Fig. 6). Extrapolated motion to the period 1 to 19 days after the earthquake (the mean epoch when postearthquake campaign measurements were made in the Andaman Islands) is about 24 cm, about 8% of the coseismic offset at nearby Port Blair. A composite time series derived from two colocated sites PORT and CAR2 (Fig. 7), spanning the interval from 10 to 100 days after the earthquake, confirms these extrapolations. Although this pertains to a restricted area of the Andaman Islands, it suggests that most of the signal in these campaign measurements is the coseismic offset, and little bias is introduced by neglecting any correction for postseismic motions in the Andaman Islands.

Nevertheless, we assess the likely postseismic motions and correct the SGPS measured offsets using a physical model. Both afterslip (e.g., Hashimoto *et al.*, 2006a,b) and asthenosphere relaxation (Pollitz *et al.*, 2006) are equally capable of explaining the observed postseismic motions. Models of both classes can be constructed that will fit the observed horizontal postseismic motions, but the two models generally yield very different patterns of vertical postseismic motions. Within the class of afterslip models, the magnitude and sign of predicted vertical offsets is sensitive to the afterslip fault geometry, in particular, the upper-edge depths of the afterslip planes. It is difficult to construct an afterslip model uniquely because there is little independent control on possible afterslip geometry apart from the PORT/CAR2 time series. Within the class of postseismic models, the magnitude and sign of predicted vertical postseismic motions depends on the distribution of slip within the elastic plate,

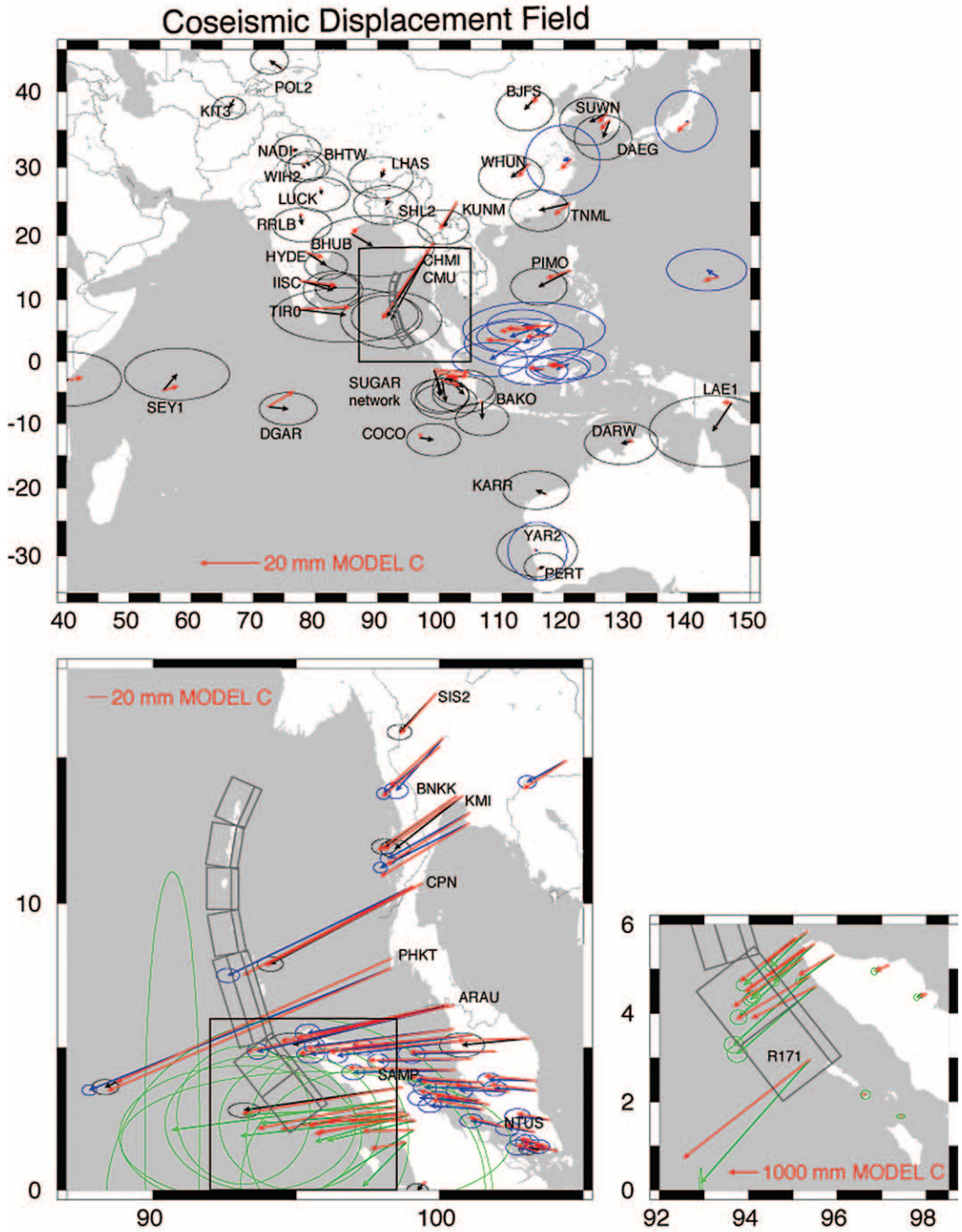

Figure 3. Coseismic horizontal displacement field of the 26 December 2004 earthquake determined in this study, shown by black vectors with 95% error ellipses, together with the "corrected" coseismic offsets derived from tables 1 and 2 of Vigny *et al.* (2005) (see text), shown by the blue vectors, and coseismic offsets derived from campaign GPS from table S1 of Subarya *et al.* (2006), shown by the green vectors. The corresponding prediction of slip-model C (Table 2), the preferred model, is shown by the red vectors. Site labels are given for those CGPS sites which are reprocessed in this study. Gray lines indicate the fault planes used to obtain Model C.

the viscoelastic structure of the asthenosphere, etc. Predicted horizontal postseismic motions from these models are more robust. We thus consider a mechanical model of postseismic motions to be useful for correcting observed horizontal offsets but not observed vertical offsets.

For simplicity we postulate that afterslip is responsible for the observed postseismic motions and construct a dislocation model that would fit the PORT/CAR2 postseismic motions. Because CAR2 has a substantial positive vertical postseismic velocity that is opposite to its coseismic offset

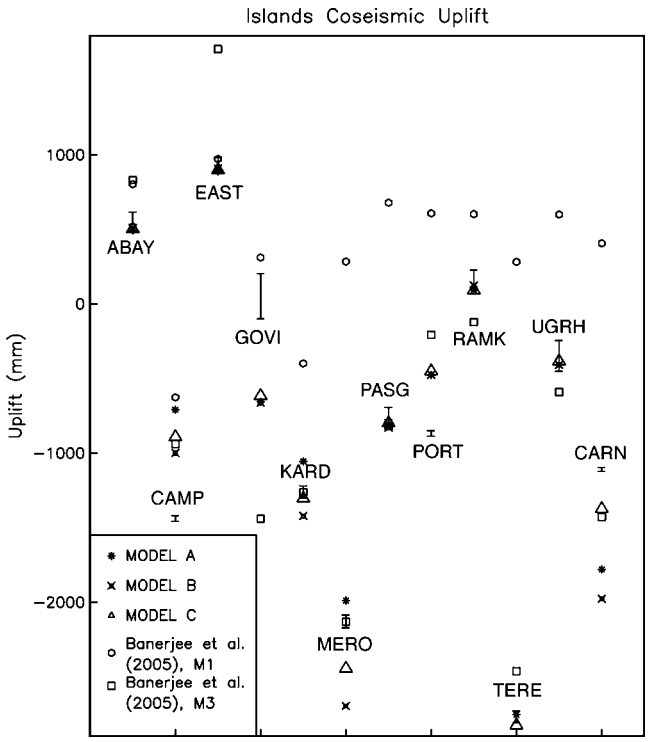

Figure 4. Vertical campaign-GPS displacements along the Andaman and Nicobar Islands determined at 11 SOI sites and at Car Nicobar (Jade *et al.*, 2005) together with various model predictions. Labels refer to site locations given in Figure 5.

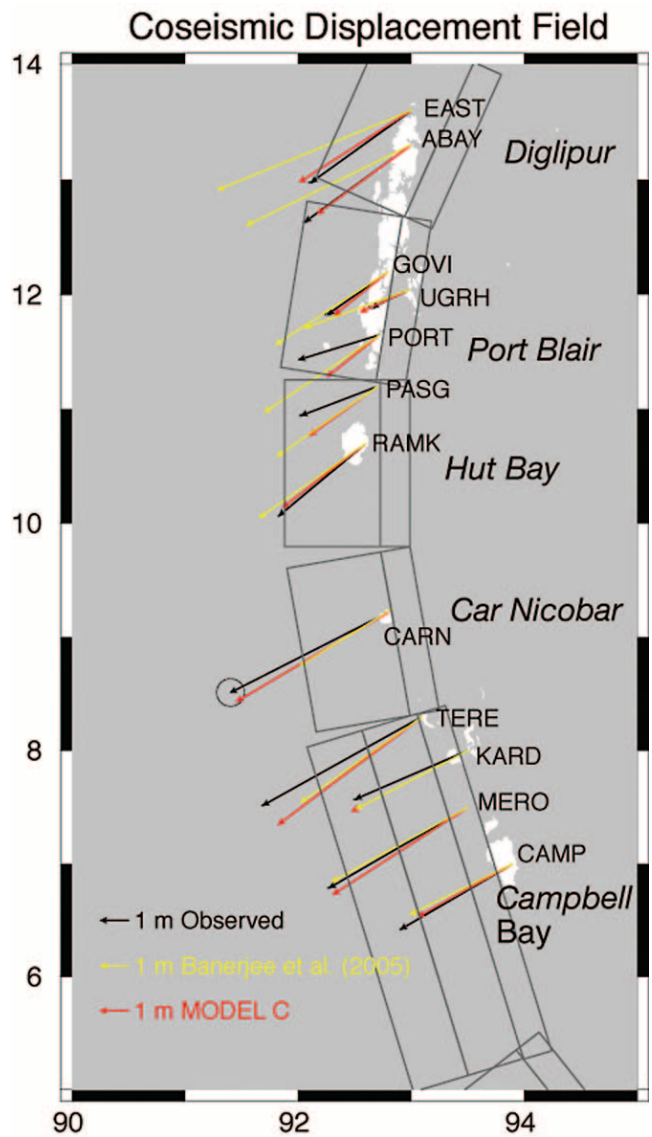

Figure 5. Horizontal near-field campaign-GPS displacements along the Andaman and Nicobar Islands determined at 11 SOI sites and at Car Nicobar (Jade *et al.*, 2005) together with the predictions of model M3 Banerjee *et al.* (2005) and model C.

(Fig. 4), the afterslip near Port Blair must be along the down-dip extension of the coseismic rupture. We assume that this applies to the entire length of the rupture and derive an afterslip model, allowing for dislocations on segments 1A, 1B, 1C, 1D, 2A, 3A, and 3B (Fig. 1 and Table 1). For simplicity we assume that afterslip on each plane is uniform, that slip is parallel to estimated coseismic slip, and that the slip values are identical on segments 1A, 1B, 1C, and 1D. Inverted afterslip and the corresponding predictions of the afterslip model are shown in Figure 6. We use this model to evaluate the motions expected at the SGPS sites during the period between the earthquake and their respective observation times, then correct the observed SGPS horizontal offsets for these motions. This amounts to a 5 to 10% reduction in westward offset for the Andaman SGPS sites, and a 1 to 10% reduction in westward offsets for Sumatran sites; in general, the reduction is about 10% for the large-offset northern Sumatran sites. We find that the resulting effect on coseismic slip models is a negligible reduction in seismic moment (less than 0.2%), suggesting that the applied correction is reasonable. (The absence of a significant effect on inferred seismic moment is because almost all uncorrected SGPS data are underpredicted by coseismic slip models, and with the previous correction model fit improves without a substantial change in inferred coseismic slip simply because the correction reduces the mismatch.) The corrected SOI and Subarya *et al.* (2006) measurements are given in Ⓔ Tables S3 and S4, respectively, in the electronic edition.

26 December 2004 Coseismic Slip Model

The fault geometry considered by Banerjee *et al.* (2005) (their table S2) is guided by aftershock activity and the seismically determined slab-depth contours (Fig. 1) and is in harmony with coseismic uplift and subsidence data from the Andaman Islands and Nicobar Islands. Within the Andaman Islands (north of about 8°) the slab-depth contours are less reliable (e.g., the actual trench axis as mapped by Curray (2005) is offset up to ~60 km to the east of the 0-km slab contour of Gudmundsson and Sambridge (1998). The fault

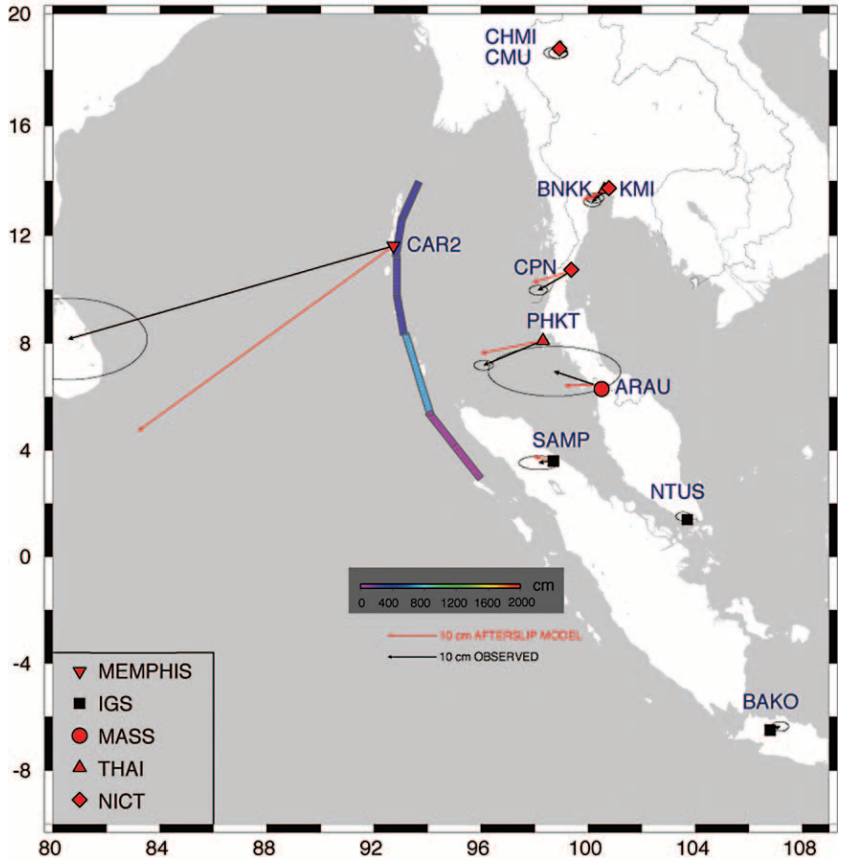

Figure 6. Horizontal displacements of various CGPS sites during the first 50 postseismic days following the Sumatra–Andaman earthquake. The estimate at CAR2 in the Andaman Islands is a logarithmic extrapolation based on data collected from days 10 to 100 after the earthquake (Fig. 7). The corresponding predictions of an afterslip model are shown with the red vectors. The slip estimated on the afterslip planes are 2.9 m (planes 1A, 1B, 1C, 1D), 6.0 m (plane 2A), 0.8 m (plane 3A), and 0.4 m (plane 3B).

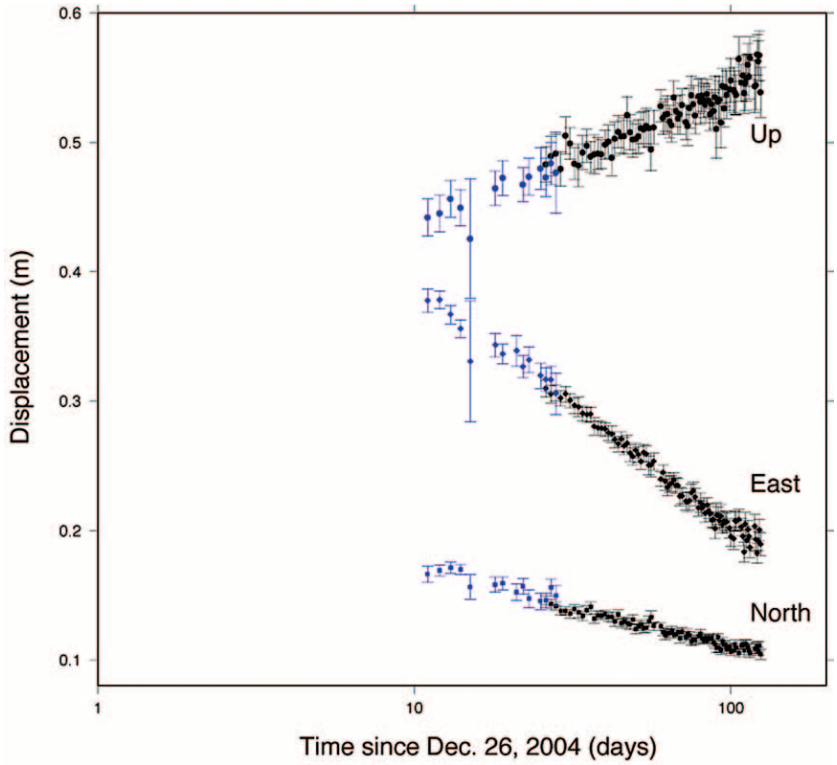

Figure 7. Composite of three-component time series collected at CGPS sites PORT and CAR2, both located at Port Blair, on a log-linear plot. Note the linear trend of each time series, conforming to a log(t) function dependence for each composite time series.

Table 1
Fault Geometry Parameters of Coseismic Rupture Planes

Segment	End Point*	d_1† (km)	d_2‡ (km)	Rake	Length (km)	Width (km)	Strike§ (°)	Dip (°)
A1	13.93° N 93.93° E	50	30	$\lambda_1 + 34°$	162.5	34.9	24	35
1B	12.65° N 93.23° E	50	30	$\lambda_1 + 17°$	162.5	34.9	7	35
1C	11.26° N 92.99° E	50	30	$\lambda_1 + 10°$	162.5	34.9	0	35
1D	9.95° N 92.99° E	50	30	λ_1	162.5	34.9	350	35
1E	14.01° N 93.55° E	30	0	$\lambda_1 + 34°$	162.5	97.1	24	18
1F	12.68° N 92.95° E	30	0	$\lambda_1 + 17°$	162.5	97.1	9	18
1G	11.26° N 92.73° E	30	0	$\lambda_1 + 10°$	162.5	97.1	0	18
IH	9.75° N 92.73° E	30	0	λ_1	162.5	97.1	350	18
2A	8.40° N 93.90° E	50	30	λ_{2A}	355	34.9	343	35
2B	8.33° N 93.05° E	30	15	λ_{2B}	355	58.0	343	15
2C	8.18° N 92.56° E	15	0	λ_{2C}	355	58.0	343	15
3A	5.51° N 94.13° E	50	30	λ_3	175	34.9	322	35
3B	4.27° N 95.11° E	50	30	λ_3	175	34.9	322	35
3C	5.35° N 93.93° E	30	0	λ_3	175	157.2	322	11
3D	4.11° N 94.95° E	30	0	λ_3	175	157.2	322	11

Variable rake is specified on the Andaman (segment 1) subsegments of variable strike such that absolute slip direction is kept constant.For a subsegment with striek ϕ and dip δ, the rake λ theoretically obeys the relationship ($\phi - 350° = \tan^{-1}(\tan\lambda\cos\delta) - \xi$, where ξ, is the azimuth of the slip direction. For simplicity we adopted and approximation $\phi - 350° = \lambda - \lambda_1$.

*Latitude and longitude of northernmost point on lower edge.

†Lower fault-edge depth.

‡Upper fault-edge depth.

§Segment strike in degrees clockwise from the north.

planes used in this study are shown in Figure 1a and described in Table 1. They are based primarily on focal mechanisms of aftershocks (Banerjee *et al.*, 2005), and near-field geodetic data. The locations of these planes are compared with hypocenter locations of earthquakes that occurred from 1915 to 2005, including aftershocks of the December 2004 event (Engdahl *et al.*, 2007), in Ⓔ Figure S4 in the electronic edition. In general, slab-related seismicity based on teleseismically determined location algorithms show much scatter and, taken in isolation, allow a modest range of possible slab geometries. The hypocenter locations in the Engdahl *et al.* (2007) catalog tend to locate systematically deeper than the chosen fault planes (equivalently, they are systematically offset to the west relative to the chosen fault planes). This is apparent in particular in the cross section for planes 1D + 1H. Rupture planes situated ~50 km to the west of the chosen planes 1D + 1H, as suggested by the Engdahl *et al.* (2007) hypocenters, are possible in this area; a model of 30 m of predominantly dip slip (rake = 105°) on plane 1H (0 to 30 km depth), after shifting it 50 km to the west of its Table 1 location, is found to match simultaneously the 6.0-m horizontal coseismic offset (Fig. 5) and the 1.1 m subsidence (Fig. 4) at CARN. The precise location of these planes is difficult to judge because fault location trades off with slip in the fitting of the geodetic data. We prefer the chosen locations of planes 1D + 1H on the grounds that the slip required to fit the CARN offsets (16.6 ms predominantly dip slip in our preferred model) is more reasonable, but the alternative location cannot be ruled out. Off northern Sumatra near 4° N, well-constrained aftershock locations based on ocean-bottom seismometer (OBS) deployment (Araki *et al.*, 2006) accurately illuminate the slab geometry. Both the OBS-relocated seismicity (figure 4 of Araki *et al.*, 2006) and the Engdahl *et al.* (2007) catalog indicate vigorous aftershock activity down to 50 km depth, supporting the conclusion of Banerjee *et al.* (2005) that coseismic rupture penetrated relatively deep in this region. The Engdahl *et al.* (2007) catalog locations agree well with the OBS-determined aftershock hypocenters in this area, and both coincide well with the segment 3C location (Fig. 1), dipping 11° from depth 0 to 30 km, but the OBS seismicity indicates a somewhat shallower dip from 30 to 50 km: about 20° compared with 35° for our segment 3A. We choose the steeper dip for consistency with Banerjee *et al.* (2005), who noted the many aftershocks in this area associated with dip ~30°.

The fit of model M3 of Banerjee *et al.* (2005) to the near-field GPS uplifts and horizontal offsets, shown in Figures 4 and 5, respectively, supports the overall prescription of fault geometry. In this study we have further revised the Banerjee *et al.* (2005) fault geometry by adding an additional possible coseismic rupture plane deep on the Nicobar segment (subsegment 2A in Table 1). Because of the limitations of the dataset used by Banerjee *et al.* (2005), they assumed uniform slip on all Andaman (segment 1) subsegments and grouped the Nicobar subsegments 2B and 2C together into one plane. Here we allow for independent slip of all tabulated subsegments, with the restriction that variable rake on the Andaman subsegments obeys the relationship given in Table 1, assuming a single relative plate motion direction for the entire segment. We also prescribe fixed $\lambda_1 = 105°$ (Banerjee *et al.*, 2005) and $\lambda_3 = 90°$, which is consistent

with the sense of slip illuminated by seismic focal mechanisms (Banerjee *et al.*, 2005).

Near-field coseismic offsets are sensitive to details that are outside the model space being considered, for example, relatively short-scale slip variations, heterogeneity in elastic structure, etc. Because such factors are not accounted for, it is not possible to fit the near-field observations to within their formal errors. Therefore we increase these errors to represent the uncertain amount of signal that lies outside the model space. We assign nominal 20-cm standard errors to east and north components of the near-field coseismic offsets (Fig. 5). (Results depend little on the assigned near-field GPS errors within generous limits.) Vertical offsets from 12 sites in the Andaman Islands (11 SOI sites and 1 site from Jade *et al.* [2005]) and 18 sites in northern Sumatra (Subarya *et al.*, 2006) that are closest to the southern termination of rupture are also used in the inversions for fault slip. Similarly to the Andaman horizontal offset estimates, we assign nominal 20 cm standard errors to all vertical offset estimates.

Slip on a subsegment is related to static surface displacement using the source-response functions calculated with the method of Pollitz (1996). This yields theoretical displacements in a layered spherical geometry with a spherical harmonic expansion, and global Earth model PREM with isotropic elastic parameters is used for this purpose. For far-field displacements, we truncate the spherical harmonic expansion at degree $l = 1000$, equivalent to a horizontal wavelength of about 40 km. For near-field displacements, we increase the accuracy of the calculation by means of a commonly employed expedient. First, the static deformation is calculated exactly on an elastic half-space using the formulae of Okada (1985). Second, the static deformation is calculated on the spherically layered structure (i.e., PREM) with an expansion up to $l = 1000$; third, it is calculated on a homogeneous sphere with an expansion up to $l = 1000$. The static deformation is a composite of that determined in steps 1 and 2 minus that determined in step 3. This procedure is valid where sphericity effects are negligible (i.e., the near-field), and it avoids the need of conducting a spherical harmonic expansion up to very large degree.

Altogether 316 data constraints are on the slip model: 286 constraints resulting from 143 horizontal GPS vectors and 30 constraints resulting from the included vertical offsets. Least-squares inversion of the dataset yields estimates of slip values for selected segments. We find that satisfactory fits to all data may be obtained without the deeper Andaman subsegments 1A, 1B, and 1C, and the deeper Nicobar segment 2A. Inversions with any of these segments, or combinations thereof, generally yield negative slip, and therefore zero slip is assigned to these subsegments in all inversions. Inversions in which slip on Sumatran segments 3A and 3C are independent yield ~25 m slip on the deeper segment 3A and ~3m slip on the shallower segment 3C, and the tradeoff in slip between the two is not well resolved. To stabilize the inversion we impose the constraint $u_{3A} = u_{3C}$. Results for three different models are given in Table 2. Models A and

Table 2

Inverted Slip Parameters of 26 December 2004 Earthquake

Model	u_{1D} (m)	u_{1E} (m)	u_{1F} (m)	u_{1G} (m)	u_{1H} (m)	u_{2B} (m)	λ_{2E} (o)	u_{2C} (m)	λ_{2C} (o)	u_{3A} (m)	u_{3B} (m)	u_{3C} (m)	u_{3D} (m)	$\chi^{2\ddagger}$
A*	0.3 ± 0.5	6.6 ± 0.2	5.6 ± 0.3	8.0 ± 0.4	16.2 ± 0.5	16.2 ± 0.3	114 ± 2	16.2 ± 0.3	114 ± 2	14.7 ± 0.4	1.0 ± 0.6	14.7 ± 0.4	9.2 ± 0.3	2.32
B	0.0 ± 0.5	6.4 ± 0.2	5.3 ± 0.3	7.4 ± 0.4	16.4 ± 0.5	0.0†	—	56.8 ± 2.0	120 ± 2	16.2 ± 0.4	3.6 ± 0.7	16.2 ± 0.4	9.1 ± 0.3	4.40
C (Preferred)	2.3 ± 0.5	6.6 ± 0.2	5.2 ± 0.3	7.8 ± 0.4	16.6 ± 0.5	19.4 ± 0.4	110 ± 2	0.0	—	15.5 ± 0.4	0.5 ± 0.6	15.5 ± 0.4	9.2 ± 0.3	2.07

u_i and λ_i denote, respectively, slip and rake on fault i. We hold fixed $\lambda_1 = 105°$ and $\lambda_3 = 90°$. Variable rake on Andaman subsegments is described in Table 1.

*Constrained such that plane 2B and plane 2C slips and rakes are equal.

†Value fixed in inversion.

‡Reduced χ^2 equal to the full χ^2 divided by N - n, where $N = 316$ is the number of data constraints and n is the number of independent parameters ($n = 10$ for all models).The slip of subsegments 3A and 3C are constrained to be equal in all inversions.

B each involve the shallow Nicobar segment 2C. In model A, the slip of the two Nicobar segments 2B and 2C are constrained to be equal ($u_{2B} = u_{2C}$), and in model B only the shallow Nicobar slip is considered ($u_{2B} = 0$, u_{2C} variable). In model C only the intermediate Nicobar slip is considered (u_{2B} variable, $u_{2C} = 0$). The two models (A and B) which involve the shallow Nicobar segment 2C have associated reduced χ^2 misfits of 2.32 and 4.40, respectively, and perform worse than model C, which involves only the intermediate Nicobar segment 2B (Fig. 8) with $\chi^2 = 2.07$. The substantially improved fit in model C is most apparent in the fit to the near-field horizontal and vertical offsets (e.g., Fig. 4). Model B, which omits the intermediate segment altogether, fits the dataset much worse despite the very large slip value $u_{2C} = 56$ m.

28 March 2005 Coseismic Slip Model

A wealth of horizontal GPS time series is available to constrain the offsets of the 28 March 2005 Nias earthquake, primarily because the source region was near the already operating SUGAR network maintained by Caltech and the Indonesian Institute of Sciences (LIPI). Several of the time series obtained for analysis of the 26 December 2004 offset continue through the time of the Nias earthquake and constrain the coseismic offsets of the Nias earthquake. These time series are augmented by measurements at other regional sites available only after the 2004 earthquake; GPS sites with time series commencing after December 2004 include BSIM, LEWK, LWHA, and PSMK of the SUGAR network. We have assembled corresponding time series at 49 regional and global sites. Time series from site SUGAR network site PBAI are shown in Figure 9: time series from nine other sites are shown in Ⓔ Figure S6 in the electronic edition. Early post-Nias deformation is as vigorous as it was immediately after the Sumatra–Andaman earthquake (Fig. 9, and Ⓔ S6 in the electronic edition). Therefore we adopt the same procedure as before for estimating the coseismic offset, that is estimation of best-fitting lines through the 18-day preseismic and 7-day postseismic portions of the time series, and evaluation of the positions on these lines at times t_0 and t_1, respectively. Examples of the preseismic and postseismic averages are given in Figures 9 and S6. Choosing $t_1 - t_0 = 1$ day, the resulting coseismic horizontal displacement field is given in Ⓔ Table S5 in the electronic edition and plotted in Figure 10.

To obtain a coseismic slip model we are guided by the fault geometry determined by Ji (2005) and the depth contours of the downgoing slab obtained by Gudmundsson and Sambridge (1998) (Fig. 1). The former prescribes a slip surface striking 325° and dipping 15° that optimally fits seismic waveforms. Since most seismic slip is restricted to the depth range 20–40 km, we choose approximately these depths for the upper- and lower-edge depths of all planes. We have slightly adjusted the slip surface defined by Ji (2005) to conform better with the local slab depth contours (Fig. 1b), and

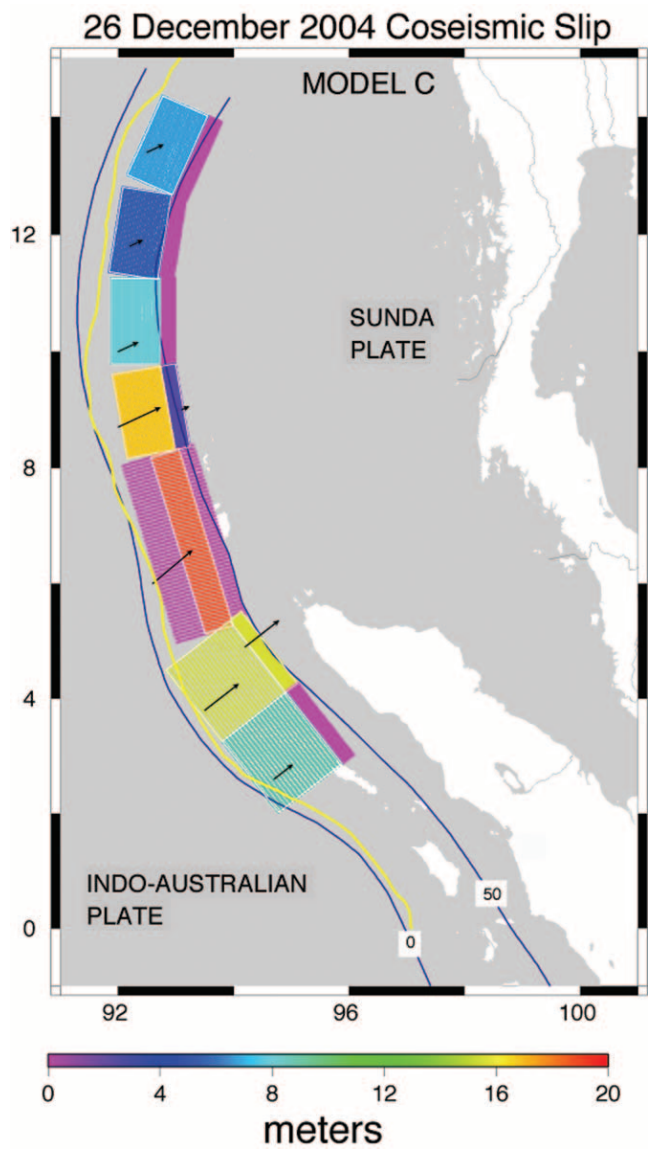

Figure 8. Coseismic slip of the Sumatra–Andaman earthquake from inversion of the integrated continuous and campaign GPS dataset using model C. Arrows indicate the motion of the footwall. Indicated are the 0 and 50 km slab depth contours of Gudmundsson and Sambridge (1998). Yellow curve is the trench axis determined by Curray (2005).

extended it in the northwest and southeast directions, resulting in five distinct slip planes (Table 3). The upper- and lower-edge depths of segment 3, in particular, were adjusted on the basis of a trial-and-error search for these depths, resulting in the best fit to the dataset, other factors being equal. The southernmost segment (segment 5) extends slightly beyond the limit of main aftershock activity (Fig. 1). The distribution of data and azimuthal coverage are such as to allow inversion for dip slip and strike slip on all segments, with the exception of the northernmost one (segment 1), on which we prescribe rake = 90°. Three of the coseismic displacement vectors—BSIM, LHWA, and PSMK (Fig. 10)—have

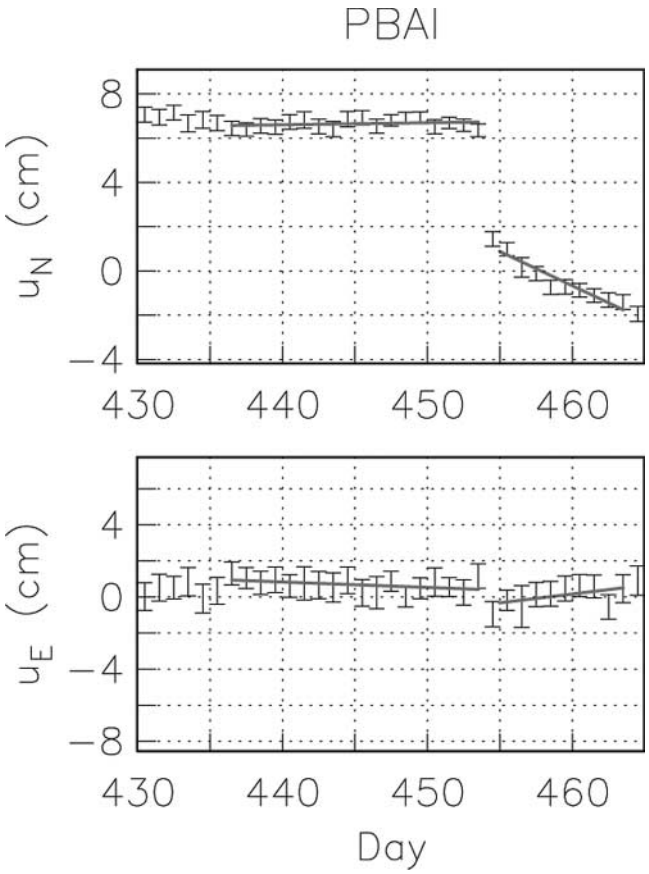

Figure 9. Observed GPS time series following the 28 March 2005 earthquake with $1-\sigma$ errors at GPS site PBAI. u_E and u_N refer to east- and northward displacement, respectively. Day numbers refer to the year 2004. Superimposed in thick gray are the straight-line fits to the 18-day portions of the preseismic and 7-day portions of the postseismic time series.

large displacements that are likely sensitive to shorter-length-scale details of the actual slip distribution than we attempt to model, and therefore the formal standard errors in the corresponding displacements are scaled up by 1 to 2 orders of magnitude. The standard deviations of north and east components of all 46 other sites are assigned their formally determined values from Ⓔ Table S4 (generally a few mm) in the electronic edition.

Least-squares inversion of this dataset for the fault-slip parameters yields the slip values and associated uncertainties given in Table 3 and plotted in Fig. 11. The slip is concentrated on the relatively deep segment 2 and relatively shallow segment 3, which accommodate about 12-m and 8-m dip slip, respectively. These slip values and the relatively shallow depth of the segment-3 slip are consistent with the slips and locations of the two most prominent slip maxima in the seismic-slip inversion of Ji (2005). Briggs *et al.* (2006) used a combintation of coral microatoll measurements and GPS displacement vectors to obtain a high-resolution slip distribution. The locations and amplitudes of their slip maxima are similar to those of Ji (2005) and agree with the locus of maximum slip between ~1° N and 2.5° N obtained in our study. The concentration of seismic-moment release between depths of 14 and 35 km, well to the east of the trench axis, obtained by Briggs *et al.* (2006) agree well with our inferred slip distribution. Our geodetically determined model, obtained with a dip of 15°, corresponds to magnitude M_w 8.66. (We use the formula $M_w = (2/3)\log_{10} M_0$ [dyne cm] − 10.7 [Hanks and Kanamori, 1979].) This is larger than the magnitude M_w 8.5 obtained by Ji (2005) from seismic-wave analysis using the same dip. This suggests a substantial difference between the moment at seismic periods and that determined geodetically, which may imply an additional contribution from afterslip occurring within a short time after the earthquake.

Reduced χ^2 associated with the slip model is 2.16. The overall fit to the dataset is better than suggested by this value because a large fraction of the misfit arises from the misfits at just three sites: SAMP, MSAI, and BSIM. For example, omission of MSAI results in a reduced χ^2 of 1.92 with nearly the same slip distribution. Improved fit of these sites may require a combination of more detailed slip on the considered planes plus possibly additional slip extending even further to the southeast. This may apply, in particular, to MSAI, which may record slip on an isolated patch near −2° N, 99° E, the site of a cluster of aftershock activity (Fig. 1) which is well removed from the main locus of slip.

Discussion of the 26 December 2004 Coseismic Slip Model

The best-fitting model is model C (hereinafter the "preferred model"), which prescribes ~19-m slip beneath the Nicobar segment from 15 to 30 km depth (Fig. 8) without any shallower or deeper slip along that segment. In addition to fitting near-field horizontal and vertical offsets better than other models, its performance also arises from fitting distant sites PHKT and ARAU better than the other models. Models A and B yield predicted displacements at PHKT that are slightly too small and displacements at ARAU that are slightly too large. The preferred model allows these offsets to be better fit by shifting the locus of displacement toward PHKT with subsegment 2B. A variation of the preferred model which solves additionally for shallow Nicobar segment slip (u_{2C}) yields almost identical slip and rake values for the other segments but a negative slip of $u_{2C} = \sim -19.5 \pm 3.2$ m on the shallow Nicobar segment, verifying that relatively low or no slip on the shallow Nicobar segment is preferred.

Deep coseismic slip beneath the Sumatra segment (segment 3) was established by Banerjee *et al.* (2005), and together with the deep slip beneath the Nicobar (2A) and southern Andaman (1D) subsegments, this suggests that slip extending well below 30 km depth characterized the overall rupture from its initiation at 3° N northward to about 9.5° N. Thereafter, the slip of the remaining ~600 km of the Andaman segment must be relatively shallow (≲30 km depth)

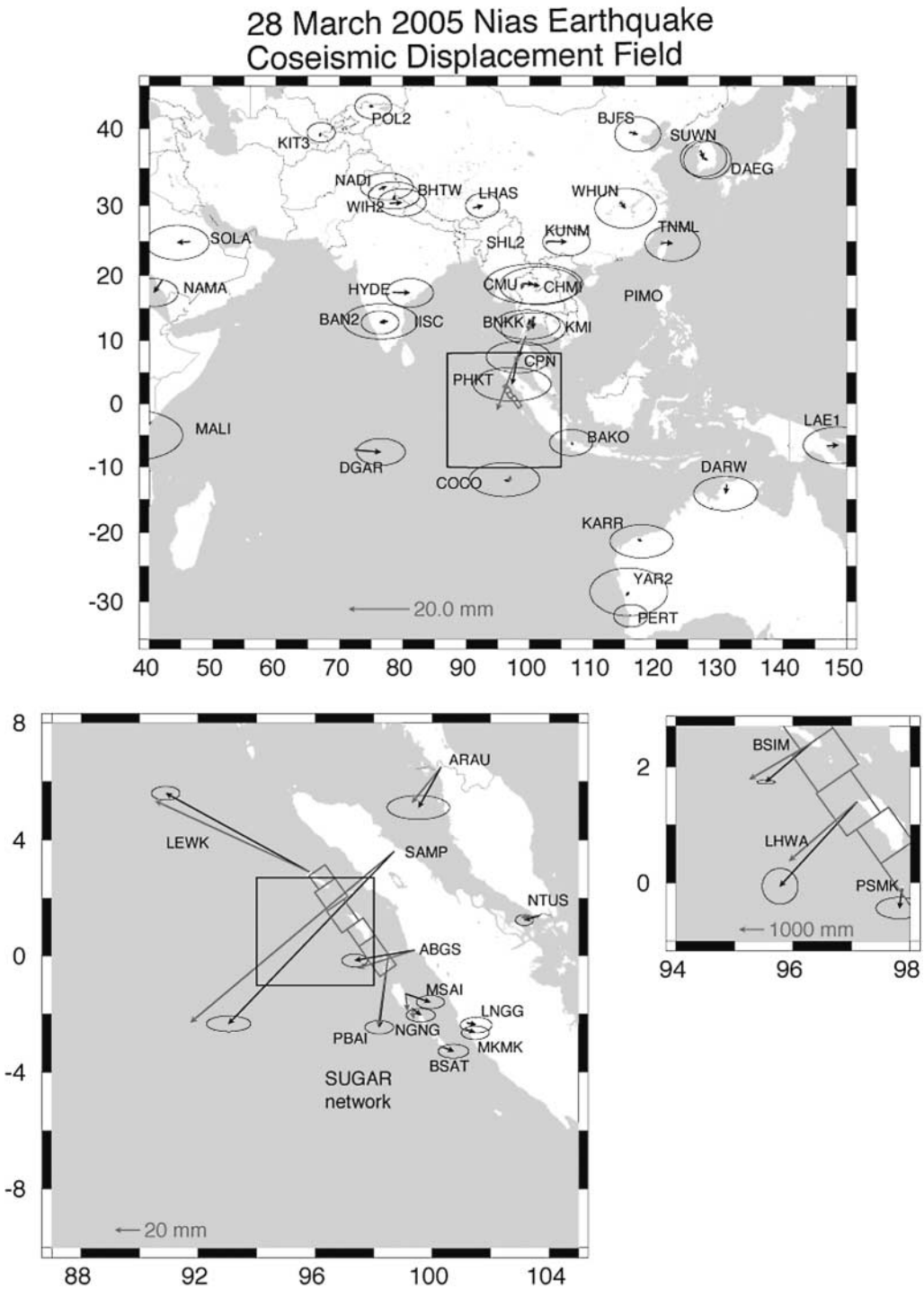

Figure 10. Coseismic horizontal displacement field of the 28 March 2005 earthquake, shown by black vectors with 95% error ellipses. Superimposed gray vectors are the predicted static displacements on the PREM model using the five-plane slip model given in Table 3. Gray lines indicate the fault planes.

to satisfactorily match the vertical GPS data. This follows from comparison of the Banerjee *et al.* (2005) model M1 and all other models in Figure 4. Model M1, which includes deep slip along the entire Andaman segment, poorly fits the observed subsidence at Port Blair and several other northern Islands sites.

The pattern of uplift predicted by the preferred model matches observed GPS uplifts on the Nicobar and Andaman

Table 3
Fault-Plane and Inverted-Slip Parameters of 28 March 2005 Nias Earthquake

Segment	End Point*	d_1† (km)	d_2‡ (km)	Length (km)	Width (km)	Strike§ (o)	Dip (o)	Slip (m)	Rake (o)
1	3.15° N 96.34° E	42	22	65	77.3	325	15	0.3 ± 0.05	90.0
2	2.67° N 96.68° E	42	17	85	96.6	325	15	12.3 ± 0.3	97 ± 0.4
3	1.95° N 96.98° E	30	9	100	81.1	325	15	8.2 ± 0.6	91 ± 4
4	1.31° N 97.63° E	42	22	80	77.3	325	15	3.1 ± 0.5	107 ± 3
5	0.72° N 98.05° E	42	22	140	77.3	325	15	0.2 ± 0.02	119 ± 15

*Latitude and longitude of northernmost point on lower edge.
†Lower fault edge depth.
‡Upper fault edge depth.
§Segment strike in degrees clockwise from due north.

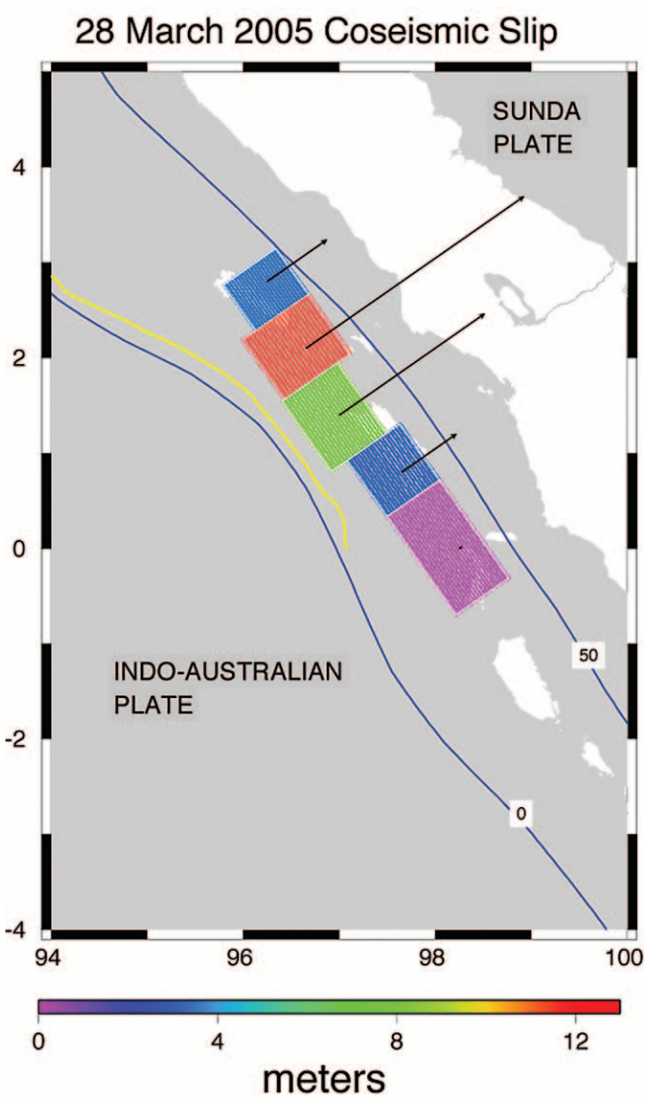

Figure 11. Coseismic slip of the Nias earthquake from inversion of the continuous GPS dataset. Arrows indicate the motion of the footwall. Indicated are the 0 and 50 km slab depth contours of Gudmundsson and Sambridge (1998). Yellow curve is the trench axis determined by Curray (2005).

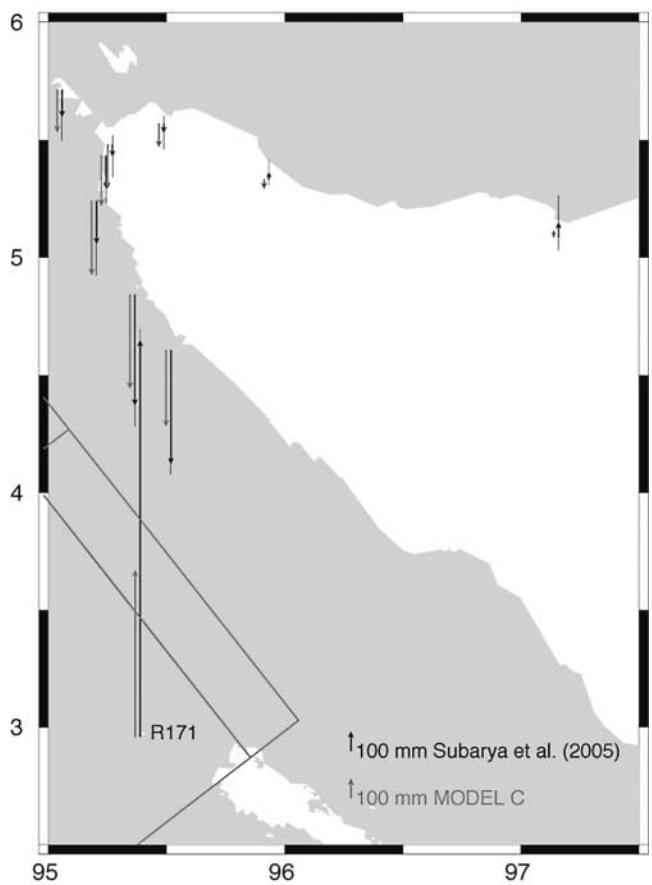

Figure 12. Predicted uplift on Sumatra–Andaman coseismic model C around northern Sumatra compared with vertical campaign-GPS displacements (Subarya *et al.*, 2006). Gray lines indicate the fault planes used to obtain model C.

Islands (Fig. 4) and around northern Sumatra (Fig. 12), and it may be compared with the uplift pattern determined by the response of corals to the change in local tide induced by the seafloor uplift/subsidence (Meltzner *et al.*, 2006). The comparison in Figure 13 includes those measurements from

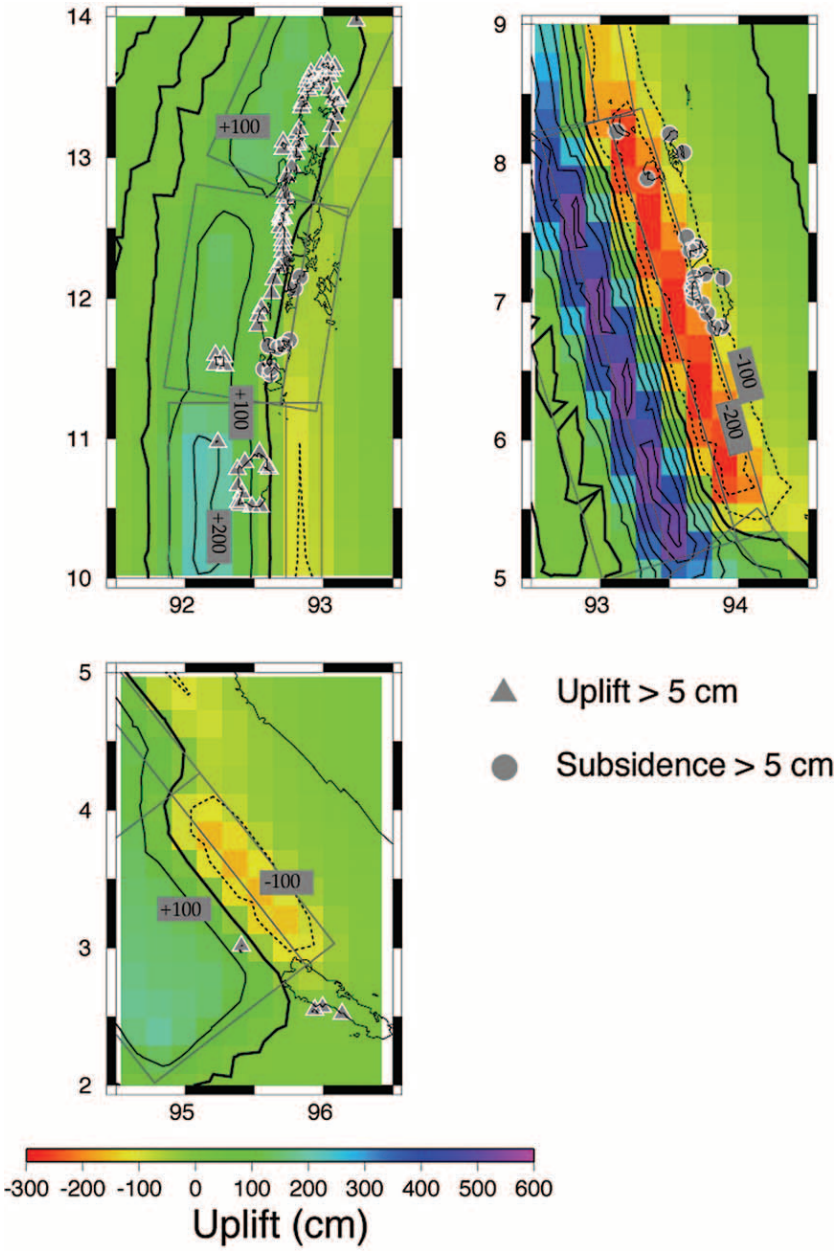

Figure 13. Predicted uplift on Sumatra–Andaman coseismic model C. Thick black lines denote zero uplift contour. Superimposed are locations of uplift (triangles) and subsidence (open circles) determined by Meltzner *et al.* (2006) with either 5 cm minimum uplift or 5 cm minimum subsidence. Gray lines indicate the fault planes used to obtain model C.

table 1 of Meltzner *et al.* (2006) indicating at least 5 cm uplift or 5 cm subsidence; in general, absolute vertical movements are not possible using satellite imagery of coral reefs. However, field investigations of reefs around Simeulue Island provide a detailed and quantitative description of the uplift patterns near the southern edge of the rupture (Meltzner *et al.*, 2006, their table 2). The sign of observed movements is generally well predicted except near Simeulue Island (about 2.5° N, 96.0° E), where a small amount of subsidence ~20 cm is predicted where small uplift ≳20 cm is measured. Small subsidence of ~6 cm is predicted just slightly further east, comparable with observed subsidence of ~50 cm at 2.392° N, 96.332° E according to table 3 of Meltzner *et al.* (2006). These results suggest that some minor slip may have continued further south to beneath Simeulue Island. Slip heterogeneity around the southernmost part of the rupture is also suggested by the three-dimensional coseismic offset at R171. The horizontal offset is shown in Figure 3 and the vertical offset in Figure 12, where they are compared with the model C prediction. The ~5.7-m horizontal offset is satisfactorily matched by the model, but the ~2.1-m uplift is underpredicted. The ratio between the vertical and horizontal offsets at R171 is much larger than expected for a site in the hanging wall of an 11°-dipping fault. Subarya *et al.* (2006) fit the three-dimensional displacement vector at R171 with a very localized slip patch which accomplishes the task of matching the large vertical-to-horizontal offset ratio.

The slip distribution on the preferred model (Fig. 8) is consistent with the results of seismic slip inversions (e.g.,

Ammon *et al.*, 2005) and joint seismic-geodetic inversion (Chlieh *et al.*, 2007). These studies employed a spherical layered Earth 3D model (Ammon *et al.*, 2005) and a layered half-space (Chlieh *et al.*, 2007), and among existing studies they are the most comparable with our results based on a spherical layered 1D Earth model. Referring to model III of Ammon *et al.* (2005) (their figure 5c) and model G-M9.15 of Chlieh *et al.* (2007) (their figure 9), these studies have fault geometry similar to that used in the present study, and slip locations and maxima in good agreement with that determined here. This includes the very deep dip slip of ~20 m near 4° N, relatively deep dip slip on the Nicobar segment from 5° N to 8° N, and a moderate amount of oblique slip (3 to ~8 m) along the Andaman Islands north of ~9° N. The slip amplitudes of Chlieh *et al.* (2007) in the Andaman Islands, in particular, match our slip amplitudes because of their use of geodetic data from this region. The persistence of high-amplitude slip (15 to 20 m) from 3° N to ~9° N is also a common feature of the model G-M9.15 of Chlieh *et al.* (2007) and the present study: estimated slip amplitudes along the Nicobar segment are about 50% smaller in model III of Ammon *et al.* (2005). This suggests that despite the vigorous aftershock activity around the shallow Nicobar segment—segment 2C (Figure 1a)—the associated coseismic slip was relatively low.

The seismic moment of the preferred model is $M_0 = 7.62 \times 10^{22}$ N m, corresponding to M_w 9.22. (Again, we use the formula $M_w = (2/3) \log_{10} M_0$ [dyne cm] $- 10.7$, the definition given by Hanks and Kanamori [1979].) Model III of Ammon *et al.* (2005) has a seismic moment of 6.5×10^{22} N m, corresponding to M_w 9.17. The apparent excess geodetic moment over the seismic moment is 17%. Ammon *et al.* (2005) find that at seismic frequencies up to 2000 sec, relatively little slip occurred on the Andaman segment. Their model, which has most seismic slip finished in about 10 min after the mainshock, is further consistent with the free oscillation spectra at periods up to one hour (Park *et al.*, 2005). Park *et al.* (2005) note that slow slip confined to the period after seismic slip terminated but up to only one hour after the mainshock would inefficiently excite the observed free oscillations because of phase cancellation. Slow slip distributed over a period of hours after seismic slip terminated, however, would have little effect on the free oscillation amplitudes, which would then be shaped primarily by the seismic slip accumulated during the first 10 min. Therefore, it is tempting to suggest that the several meters of slip on the Andaman segment, needed most notably to explain the several meters horizontal offsets at Islands sites (Fig. 5) and the apparent geodetic-seismic moment discrepancy, must have occurred at periods far greater than one hour. However, this interpretation is not supported by analysis of CGPS time series. Vigny *et al.* (2005) showed that little motion occurred at Phuket (PHKT) after about 10 min. Moreover, their various PHKT-offset estimates differ from our own estimate by only 4%. If the geodetic-seismic moment discrepancy were real, then one would expect a much larger difference. Hashimoto *et al.* (2006b) has further shown that CGPS sites in northern Thailand, which are particularly sensitive to motions along the Andaman Islands, exhibit little resolvable motions after the first 10 to 20 min. Analysis of joint seismic and geodetic datasets (Chlieh *et al.*, 2006) yields a coseismic slip model with slippage occurring during the first ~10 min and with predictions that are in harmony with both datasets. The range of seismic moment in the acceptable models of Chlieh *et al.* (2006) is 6.7 to 7.0×10^{22} N m, only 8 to 12% lower than the geodetic moment inferred in this study. (The seismic moment of their model G-M9.15 is 6.93×10^{22} N m, 9% lower than inferred in the present study.) Until direct evidence from hourly or epoch GPS solutions becomes available, we surmise that the apparent geodetic-seismic moment discrepancy is artificial or explicable with small amounts of aseismic slip beyond the first hour after the mainshock.

The remaining seismic-moment discrepancy may reflect simply the uncertainties inherent in each approach. The imaging power of each study is good based on formal resolution tests (e.g., figure 4a and 4b of Chlieh *et al.*, 2007) and the relatively small (~1–2 m) formal standard deviations of our slip estimates (Table 2). However, both the regularization used in distributed-slip inversions (Ammon *et al.*, 2005; Chlieh *et al.*, 2007) and the assumption of uniform slip on prespecified dislocation planes (this study) will inevitably result in inaccurate slip distributions, with a corresponding uncertainty of the net seismic moment estimated in each study. If far-field GPS measurements are a reliable guide to the earthquake size, we suggest that either model G-M9.15 of Chlieh *et al.* (2007) or the preferred model of the present study, each of which fit the far-field GPS data with a layered structure, provides a useful estimate of the net seismic moment.

Secondary Source in the Aceh Basin?

On the basis of tsunami amplitudes and arrival times in northwest Sumatra during the 2004 Sumatra–Andaman earthquake, Plafker *et al.* (2006) propose a secondary source in the Aceh basin. To produce the very large (up to 39 m) runups along the coast of northwest Sumatra, they envision coseismic slip on a steeply dipping splay structure accommodating ≳15 m dip slip. The proposed structure would be on the western edge of the Aceh basin, along the eastern edge of a sharp shelf break, a location that is coincident with the West Andaman Fault (Sieh and Natawidjaja, 2000). A set of aftershocks within the overriding plate is localized in this area (area C in figure 3 of Araki *et al.* [2006]). suggestive of some coseismic slip on a structure in this area. The geodetic data considered here hint at the existence of this structure through its kinematic implications. Dip slip on splay faults during the 1964 Alaska earthquake served to produce a kinematic discontinuity between the deeper megathrust and shallower magathrust such that a substantial amount of deeper slip was transferred to the splay faults,

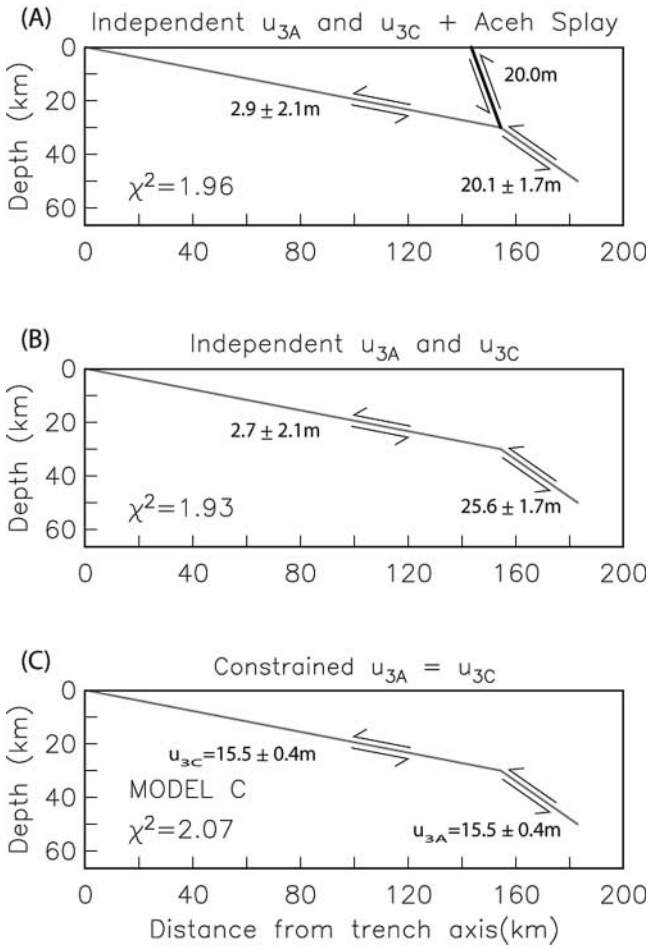

Figure 14. Estimated slip resulting from geodetic data inversions using variations of the preferred model C. Case A uses a combination of independent dip slip on segments 3A and 3C and a dip slip of 20 m prescribed on the Aceh splay. Case B allows for independent dip slip on segments 3A and 3C without the Aceh splay. Case C is Model C, which constrains the dip slip of segments 3A and 3C to be identical.

resulting in relatively little slip of the shallower megathrust (Plafker, 1969). A hypothetical splay fault located near the boundary of Sumatran segments 3A and 3C could play the same role. We summarize the results of geodetic inversions involving variations of model C in Figure 14; the result of model C itself is depicted in Figure 14c. One variation allows the dip slip of segments 3A and 3C to be independent. Resulting slip values on other segments are nearly identical with Model C slip values, but the estimated segment 3A and 3C slip values are 25.6 ± 1.7 m and 2.7 ± 2.1 m, respectively, with associated χ^2 of 1.93 (Fig. 14b). We further consider a hypothetical high-angle thrust ("splay fault" in Fig. 14a), approximately coincident with the West Andaman fault, placed with a lower edge at the upper edge of segment 3A. Fits to the geodetic data are practically insensitive to possible slip along this segment, which would involve primarily vertical motions on a fault that is distant from most of the GPS sites. When dip slip of 20 m is assigned to this segment (Fig. 14a) and remaining slip parameters are inverted as before, the result is u_{3A} = 20.1 m and u_{3C} = 2.9 m, with χ^2 = 1.96. The robust feature of these test results is the disparity in slip between segments 3A and 3C, regardless of the possible value of slip on the splay fault. The discontinuity in dip slip between segments 3A and 3C need not be as large as this, because model C yields a reasonable fit to the dataset with equal amounts of slip on both segments. However, these inversion results—which both have a significantly better fit than model C—suggest some measure of kinematic discontinuity between the deeper and shallower slip on the megathrust in this area. If real, then the disproportionate amount of aftershock activity deeper than 30 km imaged by Araki *et al.* (2006) would reflect the much greater coseismic slip having occurred along the deeper section of the megathrust.

Conclusions

We have assembled new datasets of GPS offsets for the 26 December 2004 Sumatra–Andaman and 28 March 2005 Nias earthquakes. Our compilation includes new data for 64 sites for the Sumatra–Andaman earthquake, 53 of which are continuous GPS, providing far-field measurements, and 11 of which are campaign GPS, providing near-field measurements. These data are augmented by:

1. An additional nonredundant coseismic vector offset in the Andaman Islands, one of several such vector offsets given by Jade *et al.* (2005),

2. Static offsets estimated at 55 nonredundant far-field sites by Vigny *et al.* (2005) (48 of which are continuous GPS measurements and the other 7 campaign GPS measurements in Thailand), and

3. Twenty-three northern Sumatra sites by Subarya *et al.* (2006) (all of which are campaign GPS measurements).

The 12 near-field campaign measurements and 18 of the 23 northern Sumatra campaign measurements contribute useful vertical displacements. The composite dataset has altogether 143 horizontal displacement vectors and 30 vertical displacement vectors.

All CGPS offsets are here derived by projecting the preearthquake displacements to the time just before the mainshock, and the postearthquake displacements to a time point one day after the mainshock. For the Sumatra–Andaman earthquake, the campaign data involve postearthquake motions occurring anywhere from 10 days to 7 weeks after the mainshock. Postearthquake movements during the first three weeks at Port Blair are a small fraction (about 8%) of the coseismic offset. We perform a small correction of Andaman and northern Sumatra SGPS data by deriving an afterslip model based on available CGPS time series, then evaluating the effect of this afterslip in appropriate time intervals at the SGPS sites. In this manner the SGPS data are corrected for postseismic offsets.

Our compilation also includes horizontal displacement

data for 49 sites for the Nias earthquake, all of which are continuous GPS sites. The distribution of sites with respect to the Sumatra–Andaman rupture has a preponderence of sites at distances ≳500 km from the rupture, a dearth of sites within the distance range 50 to 500 km, and a good number of sites within 50 km of the rupture in the Andaman Islands. The distribution of sites with respect to the Nias earthquake is much more uniform in terms of distance from the rupture. In both cases, the site distributions afford a fairly detailed picture of the slip distribution of each earthquake, including the centers of dominant slip and their approximate extent in depth, in approximate agreement with the results of more detailed seismic-slip inversions.

Acknowledgments

We greatly appreciate data made available by BAKO-SURTANAL (SAMP), IGS (BAKO, NTUS), the Department of Survey and Mapping Malaysia (MASS sites), Narong Hemmakorn at the King Monkut's Institute of Technology Ladkrabang, Thailand (CPN, KMI), Tharadol Komolmis, Chiang Mai University, Thailand (CHMI), Susumu Saito (NICT sites), and the Tectonics Observatory at Caltech, the Indonesian Institute of Sciences (LIPI) and Scripps Orbit and Permanent Array Center (SuGAr network). We also thank M. Hashizume for his efforts of establishing GPS monitoring stations in Thailand. John Paul (CERI Memphis) established the CGPS station CAR2. We thank Xavier Le Pichon for discussion of regional seismotectonics and George Plafker for discussion of the proposed secondary source in the Aceh Basin. This article was improved by constructive criticisms of Jean-Philippe Avouac and Jeff Freymueller.

References

Ammon, C., C. Ji, H.-K. Thio, D. Robinson, S. Ni, V. Hjorleifsdottir, H. Kanamori, T. Lay, S. Das, D. Helmberger, G. Ichinose, J. Polet, and D. Wald (2005). Rupture process of the 2004 Sumatra-Andaman earthquake, *Science* **308,** 1133–1139.

Araki, E., M. Shinohara, K. Obana, T. Yamada, Y. Kaneda, T. Kanazawa, and K. Suychiro (2006). Aftershock distribution of the 26 December 2004 Sumatra-Andaman earthquake from ocean bottom seismographic observation, *Earth Planets Space* **58,** 113–119.

Banerjee, P., F. Pollitz, and R. Bürgmann (2005). Size and duration of the great 2004 Sumatra-Andaman earthquake from far-field static offsets, *Science* **308,** 1769–1772.

Bilham, R., E. Engdahl, N. Feldl, and S. Satyabala (2005). Partial and complete rupture of the Indo-Andaman plate boundary 1847–2004, *Seism. Res. Lett.* **76,** 299–311.

Briggs, R., K. Sieh, A. Meltzner, D. Natawidjaja, J. Galetzka, B. Suwargadi, Y.-J. Hsu, M. Simons, N. Hananto, I. Suprihanto, D. Prayudi, J.-P. Avouac, L. Prawirodirdjo, and Y. Bock (2006). Deformation and slip along the Sunda megathrust in the Great 2005 Nias-Simeulue earthquake, *Science* **311,** 1897–1901.

Chlieh, M., J.-P. Avouac, V. Hjorleifsdottir, T.-R. Song, C. Ji, K. Sieh, A. Sladen, H. Hebert, L. Prawirodirdjo, Y. Bock, and J. Galetzka (2007). Coseismic slip and afterslip of the Great (M_w 9.15) Sumatra–Andaman earthquake of 2004, *Bull. Seism. Soc. Am.* **97,** no. 1A, S152–S173.

Curray, J. (2005). Tectonics and history of the Andaman Sea region, *J. Asian Earth Sci.* **25,** 187–232.

Engdahl, E., A. Villasenor, H. DeShon, and C. Thurber (2007). Teleseismic relocation and assessment of seismicity (1918–2005) in the region of the 2004 M_w 9.0 Sumatra-Andaman and 2005 M_w 8.6 Nias Island great earthquakes, *Bull. Seism. Soc. Am.* **97,** no. 1A, S43–S61.

Gahalaut, V. K., B. Nagarajan, J. K. Catherine, and S. Kumar (2006). Constraints on 2004 Sumatra-Andaman earthquake rupture from GPS measurements in Andaman-Nicobar Islands, *Earth Planet. Sci. Lett.* **242,** 365–374.

Gudmundsson, O., and M. Sambridge (1998). A regionalized upper mantle (RUM) model, *J. Geophys. Res.* **103,** 7121–7136.

Hanks, T., and H. Kanamori (1979). A moment magnitude scale, *J. Geophys. Res.* **84,** 2348–2350.

Hashimoto, M., N. Chhoosakul, M. Hashizume, S. Takemoto, H. Takiguchi, Y. Fukada, and K. Fujimori (2006a). Crustal deformations associated with the Great Sumatra-Andaman earthquake deduced from continuous GPS observation, *Earth Planets Space* **58,** 127–139.

Hashimoto, M., M. Hashizume, S. Takemoto, Y. Fukada, K. Fujimori, H. Takiguchi, M. Satomura, Y. Otsuka, and S. Saito (2006b). Postseismic deformations following the Sumatra-Andaman and Nias earthquakes detected by continuous GPS observation in SE Asia, *Seism. Res. Lett.* **77,** 289.

Herring, T. (2005). GLOBK: Global Kalman Filter VLBI and GPS analysis program, v.102. Massachusetts Institute of Technology, Cambridge, Massachusetts, and Scripps Institution of Oceanography, La Jolla, California.

Jade, S., M. Ananda, P. Kumar, and S. Banerjee (2005). Co-seismic and post-seismic displacements in Andaman and Nicobar islands from GPS measurements, *Curr. Sci.* **88,** 1980–1984.

Ji, C. (2005). Updated result of the 05/03/28 (Mw 8.5), Sumatra earthquake, http://www.gps.caltech.edu/~jichen/Earthquake/2005/sumatra/sumatra.html (last accessed December 2005).

King, R., and Y. Bock (2005). Documentation for the GAMIT GPS analysis software, release 10.2, Massachusetts Institute of Technology, Cambridge, Massachusetts, and Scripps Institution of Oceanography, La Jolla, California.

Lay, T., H. Kanamori, C. Ammon, M. Nettles, S. Ward, R. Aster, S. Beck, S. Bilek, M. Brudzinski, R. Butler, H. DeShon, G. Ekström, K. Satake, and S. Sipkin (2005). The Great Sumatra-Andaman earthquake of 26 December 2004, *Science* **308,** 1127–1132.

Meltzner, A., K. Sieh, M. Abrams, D. Agnew, K. Hudnut, J.-P. Avouac, and D. Natawidjaja (2006). Uplift and subsidence associated with the Great Aceh-Andaman earthquake of 2004, *J. Geophys. Res.* **111,** doi 10.1029/2005JB003891.

Okada, Y. (1985). Surface deformation due to shear and tensile faults in a half-space, *Bull. Seism. Soc. Am.* **75,** 1135–1154.

Park, J., T. H. Song, J. Tromp, E. Okal, S. Stein, G. Roult, E. Clevede, G. Laske, H. Kanamori, P. Davis, J. Berger, C. Braitenberg, M. Van Camp, X. Lei, H. Sun, H. Xu, and S. Rosat (2005). Earths free oscillations excited by the 26 December 2004 Sumatra-Andaman earthquake, *Science* **308,** 1139–1144.

Paul, J., R. Smalley, R. Bilham, A. Lowry, and A. Batacharjee (2005). Postseismic deformation in the central Andaman Islands, *EOS Trans. AGU* **86,** Abstract UIIB 0838.

Plafker, G. (1969). Tectonics of the March 27, 1964 Alaska earthquake, *U.S. Geol. Surv. Profess. Pap. 543-1*, 74 pp.

Plafker, G., S. Nishenko, L. Cluff, and M. Syahrial (2006). The Cataclysmic 2004 Tsunami on NW Samatra—Preliminary evidence for a near-field secondary source along the western Aceh basin, *Seism. Res. Lett.* **77,** 231.

Pollitz, F. F. (1996). Coseismic deformation from earthquake faulting on a layered spherical earth, *Geophys. J. Int.* **125,** 1–14.

Pollitz, F. F., P. Banerjee, and R. Bürgmann (2006). Postseismic relaxation following the great 2004 Sumatra-Andaman earthquake on a compressible self-gravitating Earth, *Geophys. J. Int.* **167,** 397–420.

Sieh, K., and D. Natawidjaja (2000). Neotectonics of the Sumatran fault, Indonesia, *J. Geophys. Res.* **105,** 28,295–28,326.

Stein, S., and E. Okal (2005). Speed and size of the Sumatra earthquake, *Nature* **434,** 581–582.

Subarya, C., M. Chlieh, L. Prawirodirdjo, J.-P. Avouac, Y. Bock, K. Sieh, A. Moltzner, D. Natawidjaja, and R. McCaffrey (2006). Plate-boundary deformation of the great Aceh-Andaman earthquake, *Nature* **440,** doi 10.1038/nature04522.

Vigny, C., W. Simons, S. Abu, R. Bamphenyu, C. Satirapod, N. Choosakul, C. Subarya, A. Socquet, K. Omar, H. Abidin, and B. Ambrosius (2005). GPS in SE Asia provides unforeseen insights on the 2004 megathrust earthquake, *Nature* **436,** 201–206.

Wadia Institute of Himalayan Geology
Dehra Dun, India 248001
(P.B.)

U.S. Geological Survey
Menlo Park, California 94025
(F.P.)

Geodetic and Research Branch
Survey of India
Dehra Dun, India 248001
(B.N.)

Department of Earth and Planetary Science
University of California
Berkeley, California 94720
(R.B.)

Manuscript received 9 January 2006.